Meteor-ablated Aluminum in the Mesosphere-Lower Thermosphere

John M.C. Plane[1], Shane M. Daly[1], Wuhu Feng[1,2], Michael Gerding[3] and Juan Carlos Gómez Martín[4]

[1]School of Chemistry, University of Leeds, United Kingdom.

[2] NCAS, University of Leeds, United Kingdom.

[3] Leibniz Institute of Atmospheric Physics, Kühlungsborn, Germany.

[4] Instituto de Astrofísica de Andalucía, CSIC, 18008, Granada, Spain

Corresponding author: John Plane (j.m.c.plane@leeds.ac.uk)

Key Points:

- experimental study of the reactions of AlO^+ with O and CO provides closure for the neutral and ion-molecule chemistry of meteor-ablated Al
- atmospheric model of Al is constructed by adding this chemistry and an Al meteoric source function to the WACCM chemistry-climate model
- the model predicts a nighttime AlO density of ~10 cm^{-3}, consistent with an AlO upper limit of 57 cm^{-3} determined from a lidar campaign

Abstract

The first global atmospheric model (WACCM-Al) of meteor-ablated aluminum was constructed from three components: the Whole Atmospheric Community Climate Model (WACCM6); a meteoric input function for Al derived by coupling an astronomical model of dust sources in the solar system with a chemical meteoric ablation model; and a comprehensive set of neutral, ion-molecule and photochemical reactions relevant to the chemistry of Al in the upper atmosphere. The reaction kinetics of two important reactions that control the rate at which Al^+ ions are neutralized were first studied using a fast flow tube with pulsed laser ablation of an Al target, yielding $k(AlO^+ + CO) = (3.7 \pm 1.1) \times 10^{-10}$ and $k(AlO^+ + O) = (1.7 \pm 0.7) \times 10^{-10}$ cm^3 molecule^{-1} s^{-1} at 294 K. The first attempt to observe AlO by lidar was made by probing the bandhead of the $B^2\Sigma^+(v' = 0) \leftarrow X^2\Sigma^+(v'' = 0)$ transition at λ_{air} = 484.23 nm. An upper limit for AlO of 57 cm^{-3} was determined, which is consistent with a night-time concentration of ~5 cm^{-3} estimated from the decay of AlO following rocket-borne grenade releases. WACCM-Al predicts the following: AlO, AlOH and Al^+ are the three major species above 80 km; the AlO layer at mid-latitudes peaks at 89 km with a half-width of ~5 km, and a peak density which increases from a night-time minimum of ~10 cm^{-3} to a daytime maximum of ~60 cm^{-3}; and that the best opportunity for observing AlO is at high latitudes during equinoctial twilight.

1 Introduction

The ablation of cosmic dust particles entering the Earth's atmosphere injects a range of metals into the mesosphere/lower thermosphere (MLT) region between 80 and 120 km, giving rise to layers of metal atoms and ions [*Plane et al.*, 2015]. A recent estimate of the global mass input rate of dust is 28 ± 16 t d^{-1} [*Carrillo-Sánchez et al.*, 2020]. The relative mass abundance of Al in cosmic dust should be around 1.4%, based on the Carbonaceous Ivuna (CI) chondritic abundance [*Asplund et al.*, 2009] (the CI ratio is regarded as the closest in composition to interplanetary dust [*Jessberger et al.*, 2001]). However, Al is present in the dust as a highly refractory oxide, so that only 14% of the incoming Al ablates, mostly from high speed dust particles which originate from Halley Type Comets [*Carrillo-Sánchez et al.*, 2020].

Ablated Al atoms will then react rapidly with O_2 to form AlO [*Gómez Martín et al.*, 2017]:

$$Al + O_2 \rightarrow AlO + O \qquad \Delta H^o = -14 \text{ kJ mol}^{-1} \qquad \text{(R1)}$$

with a time constant of ~300 μs at 85 km. Thus, unlike the major meteoric metals Fe, Mg and Na which occur as layers of neutral metal atoms between about 80 and 105 km, aluminum is likely to occur predominantly as a layer of AlO. There are two reasons for this conjecture. First, atomic Si is the only other major meteoric species which undergoes a fast bimolecular reaction with O_2, and a detailed model of silicon chemistry predicts that this element occurs as a layer of SiO rather than Si in the MLT [*Plane et al.*, 2016]. Second, solar-pumped fluorescence from the $AlO(B^2\Sigma^+ - X^2\Sigma^+)$ band has been observed when tri-methyl aluminum (TMA) is released in the MLT during twilight [*Rosenberg et al.*, 1964; *Johnson*, 1965; *Golomb et al.*, 1967]. Emission from the same AlO band was also observed during entry of the very bright Benešov bolide over the Czech Republic [*Borovička and Berezhnoy*, 2016].

The only aluminum species which has so far actually been observed in the background atmosphere is the $^{27}Al^+$ ion, measured using rocket-borne mass spectrometry [*Krankowsky et al.*, 1972; *Kopp*, 1997; *Grebowsky and Aikin*, 2002]. The Al^+/Fe^+ ratio between 90 – 100 km was found from a series of rocket flights to be 0.022 ± 0.005 [*Daly et al.*, 2019], which is reasonably close to the estimated Al/Fe meteoric ablation ratio of 0.037 [*Carrillo-Sánchez et al.*, 2020]. We have recently carried out a study of the kinetics of the pertinent neutral [*Gómez Martín et al.*, 2017; *Mangan et al.*, 2020] and ion-molecule [*Daly et al.*, 2019] reactions that aluminum is likely to undergo in the MLT. These studies, along with electronic structure theory calculations to elucidate likely reaction pathways, has enabled the chemical network shown in Figure 1 to be constructed. The reactions that we have measured previously are indicated with blue arrows.

In terms of ion-molecule chemistry, Al^+ mostly reacts with O_3 in the MLT (Figure 10 in *Daly et al.* [2019]) to produce AlO^+. In Section 2.1 of the present paper we describe an experimental study to measure the rate coefficients for the reactions of the AlO^+ ion with O and CO (red arrows in Figure 1):

$$AlO^+ + O \rightarrow Al^+ + O_2 \qquad \Delta H^o = -372 \text{ kJ mol}^{-1} \qquad \text{(R22)}$$

$$AlO^+ + CO \rightarrow Al^+ + CO_2 \qquad \Delta H^o = -406 \text{ kJ mol}^{-1} \qquad \text{(R23)}$$

(note that the reaction numbering follows the complete list of reactions in Table 1). These two highly exothermic reactions (the reaction enthalpies are calculated using the electronic structure method discussed in Section 2.2) control the balance between ionized and neutral aluminum because they reduce AlO^+ to Al^+, which can only undergo slow dielectronic recombination with electrons (see Figure 1).

In terms of neutral chemistry, the measured reaction kinetics indicate that AlO will initially form $OAlO_2$ and $AlCO_3$ (see Figure 11 in *Mangan et al.* [2020]). However, $AlCO_3$ may then react exothermically with O_2 to form $OAlO_2$, which in turn is likely to react with H to produce AlOH, as shown in Figure 1. Unlike other metal hydroxides such as FeOH [*Self and Plane*, 2003], NaOH [*Gómez-Martín et al.*, 2017] and CaOH [*Gómez-Martín and Plane*, 2017], AlOH is stable with respect to reaction with H and O atoms [*Mangan et al.*, 2020] and is therefore likely to be a major Al reservoir. In Section 2.2 we use electronic structure theory calculations to explore these pathways for converting AlO to AlOH.

In fact, it appears that the only process which can recycle AlOH to AlO directly is photolysis. The excited electronic states of AlOH have been studied in some detail by *Trabelsi and Francisco* [2018] (in order to explain the observed ratio of AlO to AlOH in the interstellar medium). Using high level coupled cluster theory calculations, they showed that the two photolysis channels:

$$AlOH + h\nu \rightarrow Al + OH \qquad \text{(R17a)}$$

$$\rightarrow AlO + H \qquad \text{(R17b)}$$

should have almost identical thresholds around 225 nm. Note that any Al produced via channel R17a will immediately be oxidized to AlO via reaction R1. In Section 2.3 the photodissociation rate of AlOH in the MLT is estimated.

In Section 3 we describe a set of lidar observations of the expected AlO layer. The peak absorption cross section of AlO in the B-X band at 484.23 nm was measured in our laboratory to be $\sigma(298 \text{ K}) = (6.7 \pm 1.6) \times 10^{-15}$ cm^2 molecule^{-1} [*Gómez Martín et al.*, 2017]. This cross section

is unusually large for a molecular diatomic transition, and is only a factor of 80 smaller than the cross section for atomic Fe at 372 nm used for lidar measurements of the Fe layer in the MLT. It is worth emphasizing that although chemiluminescence from FeO and NiO has been observed in the nightglow spectrum [*Evans et al.*, 2011; *Saran et al.*, 2011], no molecular metallic species has been actively detected by resonance lidar. The lidar results are then compared with an estimate of the AlO peak density determined from the lifetime of the AlO trails produced by TMA releases.

In Section 4 we incorporate into a whole atmosphere chemistry-climate model the aluminum chemistry network shown schematically in Figure 1, together with a meteoric input function for Al [*Carrillo-Sánchez et al.*, 2020]. The model simulations are then compared with observations of Al^+ and AlO.

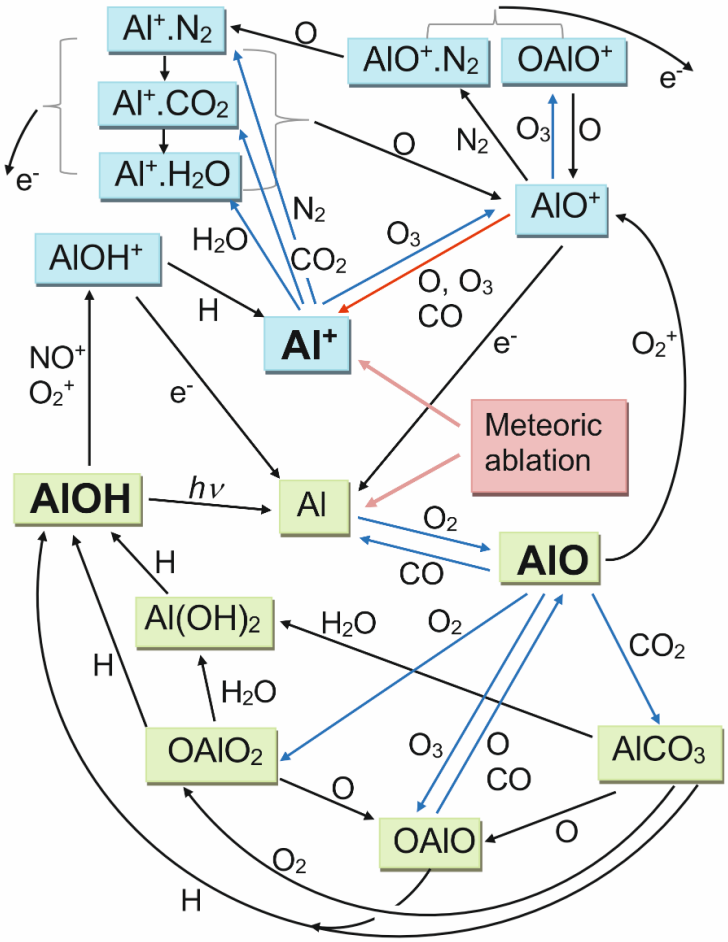

Figure 1. Schematic diagram of meteor-ablated Al chemistry in the MLT. Ionized and neutral Al species are contained in blue and green boxes, respectively. Blue arrows indicate reactions measured previously, and the red arrow shows the reactions measured in the present study.

2 Underpinning laboratory and theoretical work

2.1 Experimental study of AlO^+ reaction kinetics

Reactions R22 – R23 were studied in a stainless-steel fast flow tube which has been described in detail previously [*Daly et al.*, 2019; *Bones et al.*, 2020]. At the upstream end of the tube, a pulsed Nd:YAG laser (Continuum Surelite) was used to ablate Al^+ ions from a rotating Al rod, which were then entrained in a carrier gas flow of He (mass flow rate ranging from 3.3 - 3.5 standard liters min^{-1}). O_3 was added at a fixed injection point 19 cm downstream of the Al rod to produce AlO^+ via reaction R21 [*Daly et al.*, 2019]. Atomic O or CO was then added further downstream via a sliding injector. At the downstream end of the flow tube, after a reaction time of several milliseconds, Al^+ ions were detected with a quadrupole mass spectrometer (Hiden Analytical, model HPR60) operating in positive ion mode. A roots blower backed by a rotary pump provided a range of flow velocities from 48 – 76 m s^{-1}, at the constant pressure of 1.0 Torr which was used in these experiments. The resulting reaction times after injection of O or CO ranged from 7.5 – 8.0 ms. All experiments were conducted at 294 K.

O_3 was generated by passing O_2 through a high voltage corona discharge in a commercial ozonizer, with its concentration measured spectrophotometrically at 253.7 nm (provided by a Hg pen lamp) in a 19 cm pathlength optical cell. The O_3 absorption cross section used was 1.16×10^{-17} cm^2 $molecule^{-1}$ [*Molina and Molina*, 1986]. Atomic O was generated through microwave discharge of N_2 (McCarroll cavity, Opthos Instruments Inc.), followed by titration with NO before injection into the flow tube through the sliding injector [*Self and Plane*, 2003]. The concentration of O at the point of injection was measured by using the mass spectrometer in neutral mode to determine the amount of NO required to titrate the O. The (first-order) loss rate of O to the walls of the flow tube was measured by observing the relative change in the concentration of O ([O]) as the flight time was varied by changing the carrier gas flow rate at constant pressure. Relative [O] was monitored by adding NO downstream and recording the relative intensity of the chemiluminescence (at $\lambda > 550$ nm) produced by reaction between NO and O [*Self and Plane*, 2003].

Materials: carrier gas He (99.995%, BOC gases) was purified through a molecular sieve at 77 K before flow tube entry; N_2 (99.9999%, Air products), O_2 (99.999%, Air products) and CO (99.5% pure, Argo International) were used without further purification; NO (99.95%, Air products) was purified via 3 freeze-pump-thaw cycles before dilution in He.

2.1.1 Reaction of $AlO^+ + CO$

AlO^+ was produced by reaction with O_3 by injecting $[O_3]$ at a fixed point, and CO was then added from a sliding injector 0.5 cm downstream of the O_3 injection point. This gave a 7.5 ms reaction time from the sliding injection point to the mass spectrometer skimmer cone. k_{23} was measured by varying [CO] at a fixed $[O_3]$ of 2.73×10^{11} molecule cm^{-3}, and recording the fractional recovery of $[Al^+]$, where this is defined with respect to the $[Al^+]$ before O_3 is added. Figure 2 illustrates how this fraction increases as a function of [CO], due to R23 converting AlO^+ back to Al^+.

The flow tube kinetics are complicated by the additional reactions of AlO^+ with O_3 and O_2 [*Daly et al.*, 2019], as well as diffusional loss of the ions to the flow-tube walls. A kinetic model of the flow tube was therefore used to determine the rate coefficient k_{23}. The model uses a set of

Ordinary Differential Equations (ODEs) to describe the time-dependent variation of Al^+, AlO^+ and AlO_2^+ down the length of the flow tube. The model is described in detail elsewhere [*Bones et al.*, 2020]. The first-order wall loss rate (k_{diff}) for Al^+ was measured to be 655 ± 15 s^{-1} at 294 K and 1 Torr [*Daly et al.*, 2019]. k_{diff} for AlO^+ and AlO_2^+ were calculated to be 650 and 649 s^{-1}, respectively, from the long-range ion-induced dipole forces between these ions and the He bath gas [*Bones et al.*, 2020]. The rate coefficients and branching ratios for the reactions of Al^+ and AlO^+ with O_2 and O_3 have been measured previously by *Daly et al.* [2019], and are listed in Table 1.

A value for k_{23} was obtained by independently fitting the model to each experimental data point in Figure 2, and then calculating an overall mean value and standard deviation of k_{23} = (3.7 ± 1.1) × 10^{-10} cm^3 $molecule^{-1}$ s^{-1} at 294 K. The model run using this result is shown as the solid line in Figure 2 (the dashed lines indicate the uncertainty in k_{23}), and clearly provides a satisfactory fit to the experimental data.

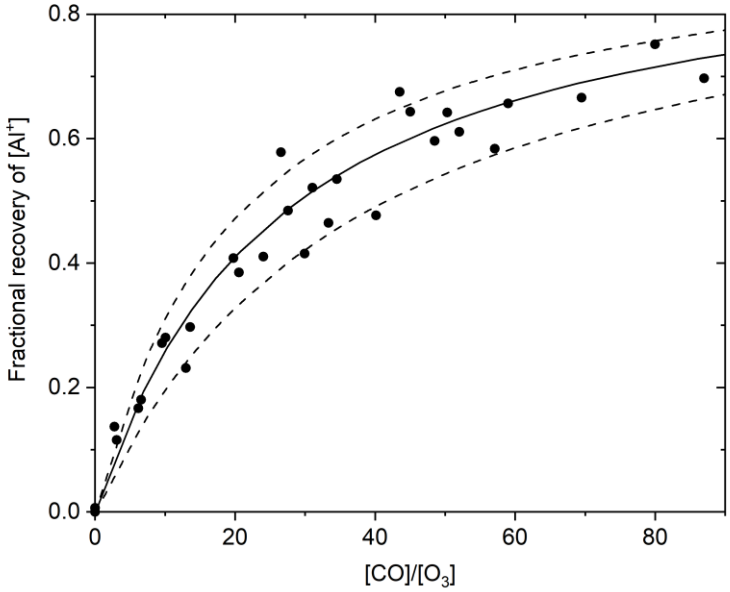

Figure 2. Fractional recovery of [Al^+] plotted against the ratio of [CO]/[O_3] in the flow tube. The solid points are the experimental data and the model fit is the solid black line, with the dashed lines illustrating the ±1σ uncertainty in k_{23}. Conditions: 1 Torr, T = 294 K.

2.1.2 Reaction of AlO^+ + O

This reaction was studied by again adding O_3 to produce AlO^+, and then injecting a constant [O] through the sliding injector. The reason for keeping [O] constant is that this reactant is more difficult to make, requiring titration of the N_2 discharge with NO and then measuring [O] at the point of injection (see above). Unlike our previous recent work on NiO^+ + O [*Bones et al.*, 2020], the reaction of the $Al^+.N_2$ cluster ion with O did not have to be accounted for in the model (the source of N_2 is the microwave discharge) because the reaction between Al^+ and N_2 is very slow [*Daly et al.*, 2019]. Figure 3 shows the Al^+ signal as a function of [O_3] (varied from (0.4 – 3.4) × 10^{11} molecule cm^{-3}), with [O] either fixed at 1.36 × 10^{13} molecule cm^{-3} (open circles) or turned off (solid circles). The flow tube kinetic model now also requires the wall loss rate for atomic O,

which was measured to be 500 ± 45 s^{-1}. The model fit (solid lines) is in good agreement with the experimental data both in the presence and absence of O, yielding k_{22}(294 K) = (1.7 ± 0.7) × 10^{-10} cm^3 $molecule^{-1}$ s^{-1}. The dashed lines illustrate the model fit with k_{22} set to its upper and lower limits at the 1σ uncertainty level.

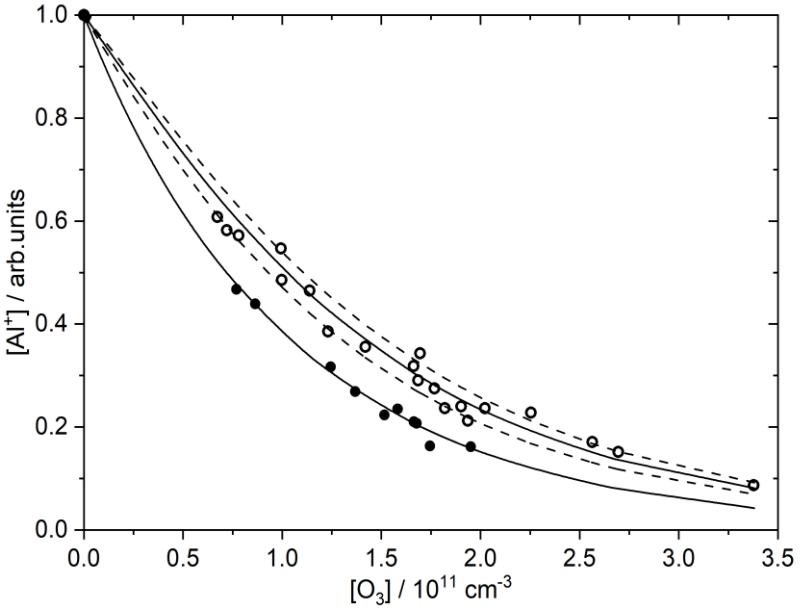

Figure 3. $[Al^+]$ as a function of $[O_3]$ in the presence of O (open circles, [O] = 1.36 × 10^{13} molecule cm^{-3}) and with the O discharge switched off (solid circles). The solid lines are model fits through the experimental data, and the dashed lines denote the ±1σ uncertainty in k_{22}. Conditions: 1 Torr, T = 294 K.

2.2 Neutral Al Chemistry

In order to explore the likely balance between AlO and AlOH in the MLT, we examine here the pathways from $OAlO_2$ and $AlCO_3$ to AlOH (Figure 1). H and H_2O have similar concentrations between 80 and 90 km [*Plane et al.*, 2015], and so direct conversion of $OAlO_2$ to AlOH (R10), and indirect conversion via $Al(OH)_2$ (R11 + R12), need to be considered:

$$OAlO_2 + H \rightarrow AlOH + O_2 \qquad \Delta H^{\ominus} = -264 \text{ kJ mol}^{-1} \qquad \text{(R10)}$$

$$OAlO_2 + H_2O \rightarrow Al(OH)_2 + O_2 \qquad \Delta H^{\ominus} = -96 \text{ kJ mol}^{-1} \qquad \text{(R11)}$$

$$Al(OH)_2 + H \rightarrow AlOH + H_2O \qquad \Delta H^{\ominus} = -168 \text{ kJ mol}^{-1} \qquad \text{(R12)}$$

Although these reactions are highly exothermic, it is important to determine whether there are any substantial energy barriers on the potential energy surfaces (PES) which link the reactants to the products. Electronic structure calculations were used to do this. The geometries of the Al-containing molecules were first optimized at the B3LYP/6-311+g(2d,p) level of theory within the Gaussian 16 suite of programs [*Frisch et al.*, 2016], and then more accurate energies determined using the Complete Basis Set (CBS-QB3) method [*Montgomery et al.*, 2000]. The potential energy surfaces for R10, R11 and R12 are illustrated in Figure 4, which also shows the geometries of the

stationary points on each surface. The Cartesian coordinates, rotational constants, vibrational frequencies and heats of formation of the relevant molecules are listed in Table S1 (Supporting Information).

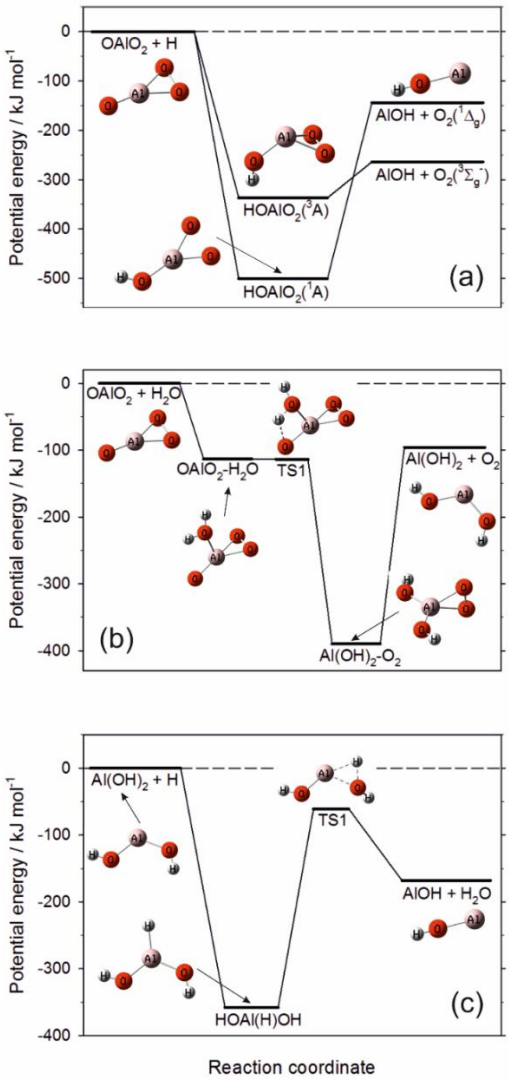

Figure 4. Reaction potential energy surfaces calculated at the CBS-QB3 level of theory: (a) $OAlO_2$ + H; (b) $OAlO_2$ + H_2O; (c) $Al(OH)_2$ + H

All three reactions exhibit deep wells on their potential energy surfaces, corresponding to very stable intermediates. However, at the low pressures of the MLT these intermediates will not be producing by collisional quenching with air molecules. There are also no barriers above the energy of the reactant entrance channels. Hence, the rate coefficients for these reactions should all be close to their collision frequencies, with small temperature dependences. Interestingly, the reaction between $OAlO_2$ and H can take place on surfaces of either singlet or triplet spin multiplicity. Although the singlet surface has a deeper well corresponding to singlet $HOAlO_2$,

spin conservation means that this species will dissociate to AlOH(^{1}A′) and electronically excited $O_2(^1\Delta_g)$.

In the case of $AlCO_3$, the most likely reaction is with O_2 to form $OAlO_2$, although reaction with H to make AlOH directly, or indirectly with H_2O via $Al(OH)_2$, are also exothermic:

$$AlCO_3 + O_2 \rightarrow OAlO_2 + CO_2 \qquad \Delta H°(0\ K) = -61\ kJ\ mol^{-1} \qquad (R14)$$

$$AlCO_3 + H \rightarrow AlOH + CO_2 \qquad \Delta H°(0\ K) = -325\ kJ\ mol^{-1} \qquad (R15)$$

$$AlCO_3 + H_2O \rightarrow Al(OH)_2 + CO_2 \qquad \Delta H°(0\ K) = -158\ kJ\ mol^{-1} \qquad (R16)$$

The potential energy surfaces for these three reactions (Figure S1-S3 in the Supporting Information) show that there are no barriers, so these reactions should also be close to their collision frequencies. In order to assign rate coefficients to R10 – R12 and R14 – R16, we assume a typical collision frequency of 2×10^{-10} cm^3 molecule^{-1} s^{-1} $(T/300)^{1/6}$ cm^3 molecule^{-1} s^{-1}, and multiply this by a statistical factor if the combination of reactant spins leads to a multiplicity of potential energy surfaces which exceeds that of the products [*Smith*, 1980]. For example, for R15 the products are both singlets, and the reactants are both doublets, so the statistical factor is (1×1)/(2×2) = 0.25. These rate coefficients are listed in Table 1.

2.3 Photochemistry of AlOH

We have shown previously that the observed growth of Fe on the underside of the mesospheric Fe layer at sunrise is most probably due to the photolysis of the reservoir species FeOH, which has a relatively large photolysis rate in the MLT of $J(FeOH) = (6 \pm 3) \times 10^{-3}$ s^{-1} [*Viehl et al.*, 2016]. Here we use the quantum chemistry method that we used previously for FeOH [*Viehl et al.*, 2016] and NiOH [*Daly et al.*, 2020] to estimate J(AlOH). First, the geometry of AlOH was optimized at the B3LYP/6-311+g(2d,p) level of theory [*Frisch et al.*, 2016]. Second, the vertical excitation energies and transition dipole moments for transitions from the AlOH ground state to the first 50 electronically excited states were calculated using the time-dependent density function theory (TD-DFT) method [*Bauernschmitt and Ahlrichs*, 1996].

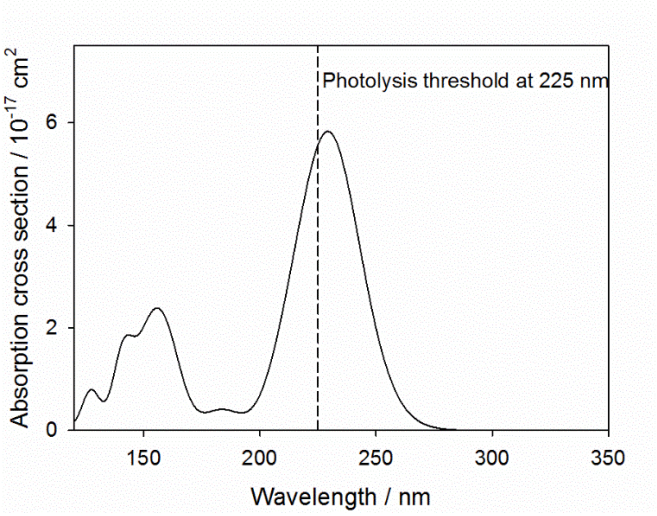

Figure 5. Absorption cross section of AlOH calculated at the TD-B3LYP//6-311+g(2d,p) level of theory. The dashed line indicates the threshold for photodissociation to Al + OH or AlO + H.

The resulting absorption spectrum is plotted in Figure 5, which shows that the threshold for photodissociation occurs close to the peak of a strong near-UV absorption band peaking at 229 nm. If absorption at wavelengths shorter than 225 nm causes photodissociation to either Al + OH or AlO + H [*Trabelsi and Francisco*, 2018], then convolving the AlOH cross section up to this threshold with the solar actinic flux from the semi-empirical SOLAR2000 model [*Tobiska et al.*, 2000] (averaged over a solar cycle), yields $J(\mathrm{AlOH}) = 3.3 \times 10^{-3}$ s^{-1} in the MLT.

2.4 Al ion-molecule chemistry

The ionization energies of AlO and AlOH are 9.82 eV [*Clemmer et al.*, 1992] and 8.89 eV [*Sikorska and Skurski*, 2009], respectively. These are both lower than the ionization energy of O_2 (12.07 eV), which means that both AlO and AlOH should charge transfer with ambient E region O_2^+ ions (R18 and R19). However, the lower ionization energy of NO (9.26 eV) means that only AlOH will charge transfer with ambient NO^+ (R20). The rate coefficients for these reactions are set to their Langevin capture rates, increased to account for the significant dipole moments of AlO (4.45 D [*Bai and Steimle*, 2020]) and AlOH (0.97 D [*Sikorska and Skurski*, 2009]) using the statistical adiabatic model of *Troe* [1985]. These capture rates are then multiplied by a statistical factor to take account of the spin multiplicities of reactants and products.

Al^+ reacts most rapidly with O_3 (R21 in Table 1) throughout the MLT [*Daly et al.*, 2019]. AlO^+ is then most likely to react with O and be reduced back to Al^+ (R22, see Section 2.1). However, AlO^+ can also recombine with N_2 (R33 in Table 1). The rate coefficient k_{33} was calculated using the version of Rice Ramsperger Markus Kassel (RRKM) theory described in *Daly et al.* [2019]. The relevant molecular parameters are listed in Table S4. This reaction is reasonably fast because the $AlO^+.N_2$ cluster ion is bound by 106 kJ mol^{-1}. It is then likely to react with O to form the weakly bound $Al^+.N_2$ ion, which can ligand switch with CO_2 and H_2O to form more stable $Al^+.CO_2$ and $Al^+.H_2O$ cluster ions [*Daly et al.*, 2019]. Note that all three of these cluster ions can also form directly through the recombination of Al^+ with N_2, CO_2 or H_2O (R27 – R29), though only the $Al^+ + N_2$ reaction is within two orders of magnitude of reaction with O_3 (R21) [*Daly et al.*, 2019]. The three cluster ions can then be converted to AlO^+ by reaction with O (R30 – R32).

The rate coefficients of all the relevant bimolecular ion-molecule reactions which have not been measured (black arrows in Figure 1) are set to their Langevin capture rates [*Smith*, 1980]. The molecular Al-containing ions can all undergo dissociative recombination with electrons (R35). These reactions are all set to the rate coefficient measured for $FeO^+ + e^-$ [*Bones et al.*, 2016], based on the observation that dissociative recombination reactions of small molecular ions nearly all have rate coefficients within a factor of 2 of 3×10^{-7} cm^3 molecule^{-1} s^{-1} [*Florescu-Mitchell and Mitchell*, 2006].

2.5 Permanent removal of Al species

Reaction R36 in Table 1 is a set of polymerization reactions which account for the permanent loss of the significant neutral Al-containing molecules AlO, AlOH and, to a lesser extent, $Al(OH)_2$ (see Section 4) to form meteoric smoke particles. We have used this type of reaction in previous models of the Na [*Marsh et al.*, 2013], K [*Plane et al.*, 2014], Fe [*Feng et al.*, 2013], Mg [*Langowski et al.*, 2015], SiO [*Plane et al.*, 2016], Ca [*Plane et al.*, 2018] and Ni [*Daly et al.*, 2020] layers. In this case, k_{36} is set to 6×10^{-8} cm^3 s^{-1}, which is ~80 times larger than a typical dipole-dipole capture rate for these metallic molecules. This factor allows for the Al-

containing reservoir species to polymerize with other metal-containing molecules produced by meteoric ablation (e.g., FeOH and $Mg(OH)_2$), whose concentration will be around 80 times higher because the elemental ablation ratio of Al atoms to the sum of Na + Fe + Mg +Si + Ni + Al atoms is 1/81.2 [*Carrillo-Sánchez et al.*, 2020].

3 Observations of AlO in the MLT

3.1 Lidar observations

3.1.1 Lidar and calibration cell setup

The absolute absorption cross section of AlO at the bandhead of the $B^2\Sigma^+(v' = 0)$ - $X^2\Sigma^+(v'' = 0)$ transition at λ_{air} = 484.23 nm is σ(298 K, 1 hPa) = $(6.7 \pm 1.6) \times 10^{-15}$ cm^2 $molecule^{-1}$ (0.003 nm resolution) [*Gómez Martín et al.*, 2017]. Because this cross section is unusually large for a diatomic molecule, we carried out a lidar campaign to determine if an AlO layer could be detected. Soundings were performed at Kühlungsborn, Germany (54°N, 12°E) for 3 nights during January 2016 and 3 nights in April 2017, yielding ~20 hours of integration time. Details of the lidar system are given by *Gerding et al.* [2019]; the instrument is a modification from an earlier twin dye laser design [*Alpers et al.*, 1996; *Gerding et al.*, 2000]. Laser emission at 484.23 nm was produced using a XeCl excimer laser at 308 nm (repetition rate = 30 Hz) to pump a dye laser with Coumarin 102 dye dissolved in methanol, producing laser radiation over the 455 – 495 nm spectral range.

A small-scale version of the flow tube used by [*Gómez Martín et al.*, 2017] was installed next to the lidar as an AlO calibration cell, both to check the laser wavelength before atmospheric measurements and then to avoid drift away from the AlO bandhead during operation. AlO was produced in the cell by laser ablation of a rotating Al rod, using 532 nm light that was beam-split from a Nd:YAG laser in the co-located Rayleigh-Mie-Raman (RMR) lidar [*Gerding et al.*, 2016]. The Al was entrained in a flow of N_2 (total pressure = 2.1 Torr), and a trace of O_2 added N_2 downstream to make AlO via reaction 1. A quartz fiber was used to guide the 484 nm laser light from the AlO lidar to the calibration cell, and laser induced fluorescence detected with a photomultiplier orthogonal to the laser beam. The dye laser was scanned in 1 pm intervals to find the peak of the AlO bandhead. A flip mirror was used to alternately direct the dye laser to the calibration cell or to the optics in the lidar transmitter.

3.1.2 Observations at 484 nm

Figure 6a shows the integrated lidar backscatter profile at 484.23 nm (blue line), summed over the 3 sounding nights during April 2017. The background noise level, which was determined by averaging the signal from 120 – 150 km (dashed line in Figure 6a), has been subtracted. The RMR lidar (green line in Figure 6), which operated simultaneously alongside the AlO resonance lidar, was used to provide an off-resonance measurement (at 532 nm) since no off-resonance measurements were taken with the resonance lidar (which was set to the AlO bandhead). Both profiles showed a monotonic decay of the Rayleigh scatter into the background noise. The 484 nm Rayleigh scatter was detected well above 80 km where an AlO layer would be expected (Figure 6b), based on the metal atom layers [*Plane*, 2003; *Gerding et al.*, 2019].

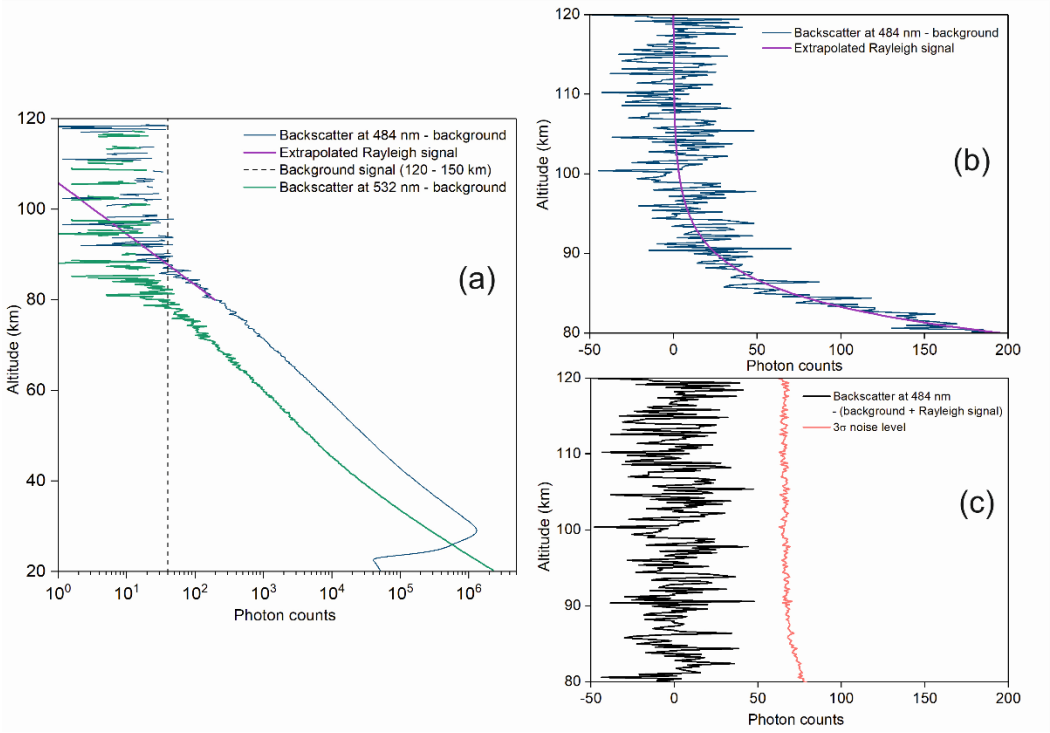

Figure 6. Integrated backscatter profile of lidar soundings during April 2017 on a log scale. (a) 484 nm lidar (blue line) and RMR lidar (green), after background subtraction. The dashed line is the 484 nm background signal measured between 120 and 150 km. The purple line is the extrapolated Rayleigh backscatter above 80 km. (b) The 484 nm lidar – background (blue line) and the extrapolated Rayleigh signal (purple line) on a linear scale. (c) Residual signal after the background and extrapolated Rayleigh backscatter are subtracted from the 484 nm signal. The red line is the 3σ photon noise level. The altitude resolution is 200 m.

The Rayleigh backscatter was then extrapolated from 80 km to higher altitudes (purple lines in Figure 6a and 6b) and subtracted from the backscatter signal to yield the residual signal (black line in Figure 6c). No obvious resonance layer was detected over the observation period; application of Poisson statistics shows that an AlO resonance signal was not present above the the 3σ photon noise threshold (red line in Figure 6c) [*Gerrard et al.*, 2001]. Nevertheless, an upper limit for the AlO density can be estimated. A Gaussian profile for the AlO layer was assumed, extending from 85 to 100 km with a peak at 90 km (analogous to other metal layers [*Plane*, 2003]), and fitted to the residual signal. Adapting the work of *Tilgner and von Zahn* [1988], the upper limit to the AlO density, n_z(AlO), is then given by:

$$n_z(AlO) = n_{zr}(air)\frac{\sigma_{Ray}(air)}{\sigma_{res}(AlO)}\frac{z^2(AlO)}{z_r^2}\frac{C(AlO)}{C(air)}\frac{1}{Tr^2(z_r,z)} \quad \text{(I)}$$

where n_{zr}(air) is the air density at the reference altitude from NRLMSISE-00 [*Picone et al.*, 2002], σ_{Ray} (7.6×10^{-27} cm^2 molecule^{-1}) and σ_{res} ((6.7 ± 1.6) × 10^{-15} cm^2 molecule^{-1} [*Gómez Martín et al.*, 2017]) are the Rayleigh and effective resonance AlO cross sections, z the altitude taken for the AlO peak, z_r the reference altitude of 30 km, C(AlO) and C(air) are the AlO resonance and Rayleigh photon counts after the background noise is subtracted, and Tr (z_r, z) is

the transmission (assumed to be 1) of the atmosphere between z_r and z at the laser pulse wavelength. This yields an AlO detection limit of 57 cm^{-3}.

3.2 Al releases in the MLT

TMA grenade releases from rocket payloads in the MLT generate visible chemiluminescence [*Golomb et al.*, 1967; *Roberts and Larsen*, 2014], which was proposed to arise from the radiative recombination reaction [*Golomb and Brown*, 1976; *Gole and Kolb*, 1981]:

$$AlO + O \rightarrow OAlO + h\nu \qquad \Delta H°(0\ K) = -390\ kJ\ mol^{-1} \qquad (R36)$$

R36 is sufficiently exothermic to produce emission at wavelengths longer than 306 nm. The OAlO product is then recycled to AlO by reaction with O:

$$OAlO + O \rightarrow AlO + O_2 \qquad \Delta H°(0\ K) = -107\ kJ\ mol^{-1} \qquad (R3)$$

which proceeds close to the capture rate [*Mangan et al.*, 2020], so that AlO is in a large excess over OAlO and the intensity of the chemiluminescence is a marker for the AlO concentration. *Roberts and Larsen* [2014] reported that the chemilumiscence intensity decayed with an e-folding lifetime of around 29 min between 90 and 100 km i.e. the first-order removal for AlO into a long-lived reservoir is ~6×10^{-4} s^{-1}. The rate of injection of Al atoms into the MLT has recently been estimated to be 3×10^{-3} cm^{-3} s^{-1} [*Carrillo-Sánchez et al.*, 2020]; since the Al will immediately be oxidized by O_2 to AlO, this represents the injection rate of fresh AlO. Balancing injection against removal, the steady-state concentration of AlO should then be ~5 cm^{-3}. This is 1 order of magnitude lower than the upper limit for AlO determined from the lidar observations in Section 3.1. Note that this estimate of the AlO density is during *night-time*, when these rocket release experiments were conducted.

4 Model simulations of Al chemistry in the MLT

4.1 WACCM-Al set up

The Al reactions in Table 1 were imported into the Whole Atmosphere Community Climate Model (WACCM6), which uses the framework developed from the second iteration of the fully coupled Community Earth System Model (CESM2) [*Gettelman et al.*, 2019]. WACCM6 has a vertical extension from the Earth's surface to the lower thermosphere at ~140 km. Although the model can be nudged by a reanalysis dataset, as we have done with other meteoric metals where measurements are available for comparison [*Plane et al.*, 2015; *Plane et al.*, 2018], for the present study we used a free-running version of WACCM6 with a reduced tropospheric chemical mechanism. The model has a horizontal resolution of 1.9° latitude × 2.5° longitude, and 70 vertical model layers (~3 km vertical resolution in the MLT region). This version of WACCM6 with Al chemistry is termed WACCM-Al. The full set of Fe reactions in WACCM-Fe [*Feng et al.*, 2013; *Viehl et al.*, 2016] was also included in order to compare model simulations with measurements of Al^+ and Fe^+ in the MLT. The model simulations were performed from 1979 to 2014, using the standard WACCM6 initialization conditions file [*Danabasoglu et al.*, 2020]. Here we focus on a decade of model output from 2004-2014, which is sufficiently long to produce a climatology of the Al species.

414 **Table 1.** Aluminum chemistry in the MLT

No.	Reaction	Rate coefficient [a]
	Neutral reactions	
R1	$Al + O_2 \rightarrow AlO + O$	$k_1 = 1.7 \times 10^{-10} (T/300)^{1/6}$ [b]
R2	$AlO + O_3 \rightarrow OAlO + O_2$	$k_2 = 1.3 \times 10^{-10} (T/300)^{1/6}$ [c]
R3	$OAlO + O \rightarrow AlO + O_2$	$k_3 = 1.9 \times 10^{-10} (T/300)^{1/6}$ [c]
R4	$OAlO + CO \rightarrow AlO + CO_2$	$k_4 = 2.6 \times 10^{-11} (T/300)^{1/6}$ [c]
R5	$AlO + CO \rightarrow Al + CO_2$	$k_5 = 2.0 \times 10^{-12} (T/300)^{1/6}$ [c]
R6	$AlO + O_2 (+ N_2) \rightarrow OAlO_2$	$\log_{10}(k_6) = -35.137 + 6.1052 \log_{10}(T) - 1.4089 (\log_{10}(T))^2$ [c]
R7	$AlO + CO_2 (+ N_2) \rightarrow AlCO_3$	$\log_{10}(k_7) = -38.736 + 8.7342 \log_{10}(T) - 2.0202 (\log_{10}(T))^2$ [c]
R8	$OAlO_2 + O \rightarrow OAlO + O_2$	$k_8 = 1.2 \times 10^{-10} (T/300)^{1/6}$ [d]
R9	$OAlO + H \rightarrow AlOH + O$	$k_9 = 2 \times 10^{-10} (T/300)^{1/6}$ [d]
R10	$OAlO_2 + H \rightarrow AlOH + O_2$	$k_{10} = 2 \times 10^{-10} (T/300)^{1/6}$ [d]
R11	$OAlO_2 + H_2O \rightarrow Al(OH)_2 + O_2$	$k_{11} = 2 \times 10^{-10} (T/300)^{1/6}$ [d]
R12	$Al(OH)_2 + H \rightarrow AlOH + H_2O$	$k_{12} = 5 \times 10^{-11} (T/300)^{1/6}$ [d]
R13	$AlCO_3 + O \rightarrow OAlO + CO_2$	$k_{13} = 4 \times 10^{-11} (T/300)^{1/6}$ [d]
R14	$AlCO_3 + O_2 \rightarrow OAlO_2 + CO_2$	$k_{14} = 6.6 \times 10^{-11} (T/300)^{1/6}$ [d]
R15	$AlCO_3 + H \rightarrow AlOH + CO_2$	$k_{15} = 5 \times 10^{-11} (T/300)^{1/6}$ [d]
R16	$AlCO_3 + H_2O \rightarrow Al(OH)_2 + CO_2$	$k_{16} = 2 \times 10^{-10} (T/300)^{1/6}$ [d]
R17	$AlOH + h\nu \rightarrow AlO + H$	$k_{17} = 3.3 \times 10^{-3}$ [e]
	Ion-molecule reactions	
R18	$AlO + O_2^+ \rightarrow AlO^+ + O_2$	$4.1 \times 10^{-9} (T/300)^{-0.364}$ [f]
R19	$AlOH + O_2^+ \rightarrow AlOH^+ + O_2$	$2.3 \times 10^{-9} (T/300)^{-0.165}$ [f]
R20	$AlOH + NO^+ \rightarrow AlOH^+ + NO$	$1.7 \times 10^{-9} (T/300)^{-0.22}$ [f]
R21	$Al^+ + O_3 \rightarrow AlO^+ + O_2$	1.4×10^{-9} [g]
R22	$AlO^+ + O \rightarrow Al^+ + O_2$	1.7×10^{-10} [h]

R23	$AlO^+ + CO \rightarrow Al^+ + CO_2$	3.7×10^{-10} [h]
R24a	$AlO^+ + O_3 \rightarrow OAlO^+ + O_2$	4.1×10^{-10} [g]
R24b	$AlO^+ + O_3 \rightarrow Al^+ + 2O_2$	8.8×10^{-10} [g]
R25	$OAlO^+ + O \rightarrow AlO^+ + O_2$	3.5×10^{-10} [f]
R26	$AlOH^+ + H \rightarrow Al^+ + H_2O$	1.7×10^{-10} [f]
R27	$Al^+ + N_2 (+N_2) \rightarrow Al^+.N_2$	$\log_{10}(k) = -27.9739 + 0.05036\log_{10}(T) - 0.60987(\log_{10}(T))^2$ [g]
R28	$Al^+ + CO_2 (+N_2) \rightarrow Al^+.CO_2$	$\log_{10}(k) = -33.6387 + 7.0522\log_{10}(T) - 2.1467(\log_{10}(T))^2$ [g]
R29	$Al^+ + H_2O (+N_2) \rightarrow Al^+.H_2O$	$\log_{10}(k) = -24.7835 + 0.018833\log_{10}(T) - 0.6436(\log_{10}(T))^2$ [g]
R30	$Al^+.N_2 + O \rightarrow AlO^+ + N_2$	1.2×10^{-10} [f]
R31	$Al^+.CO_2 + O \rightarrow AlO^+ + CO_2$	1.2×10^{-10} [f]
R32	$Al^+.H_2O + O \rightarrow AlO^+ + H_2O$	1.2×10^{-10} [f]
R33	$AlO^+ + N_2 (+N_2) \rightarrow AlO^+.N_2$	$2.7 \times 10^{-27} (T/300)^{-2.31}$ [i]
R34	$AlO^+.N_2 + O \rightarrow Al^+.N_2 + O_2$	3×10^{-10} [f]
R35	$Al^+.X + e^- \rightarrow Al + X$	$3 \times 10^{-7} (T/300)^{-0.5}$ [j]
	Sink polymerization reactions	
R36	$AlX + AlY \rightarrow Al_2XY$ (X, Y = O, OH, $(OH)_2$)	5.8×10^{-7} [k]

[a] Units: s^{-1} for photolysis reactions; cm^3 $molecule^{-1}$ s^{-1} for bimolecular reactions; cm^6 $molecule^{-2}$ s^{-1} for termolecular reactions. [b] *Gómez Martín et al.* [2017]. [c] *Mangan et al.* [2020]. [d] set to a collision frequency of $2 \times 10^{-10} (T/300)^{1/6}$ cm^3 $molecule^{-1}$ s^{-1}, scaled by a statistical electronic branching factor (see text). [e] Calculation from electronic structure theory, this study. [f] Set to the Langevin collision frequency, scaled by a statistical electronic branching factor (see text). [g] *Daly et al.* [2019]. [h] Measured, this study. [i] RRKM calculation (see text). [j] Set to the measured rate coefficient for $FeO^+ + e^-$ [*Bones et al.*, 2016]. [k] See text.

4.2 Al meteoric input function

The global average injection profiles of Al and Fe are illustrated in Figure 7. These Meteoric Input Functions (MIFs) were estimated by combining the new version of the Chemical ABLation MODel (CABMOD-3), which simulates the ablation of the major meteoric elements from an individual dust particle [*Carrillo-Sánchez et al.*, 2020], with the Zodiacal Cloud Model (ZoDY)

which provides the mass, velocity and radiant distributions of particles entering Earth's atmosphere from Jupiter Family Comets, the asteroid belt, and long-period Halley-Type comets [*Nesvorný et al.*, 2011]. The contributions from these different sources are weighted using the procedure in *Carrillo-Sánchez et al.* [2016].

Note that both injection profiles in Figure 7 have been reduced by a factor of 5 from the profiles in *Carrillo-Sánchez et al.* [2020]. This accounts for the fact that global models such as WACCM underestimate the vertical transport of minor species in the MLT, because short wavelength gravity waves are not resolved on the current horizontal grid scale of the model (~220 km). These sub-grid waves contribute to vertical chemical and dynamical transport of constituents while dissipating, and this can exceed transport driven along mixing ratio gradients by the turbulent eddy diffusion produced once the waves break [*Gardner et al.*, 2017]. Because these additional vertical transport mechanisms are underestimated, the MIF of each metal needs to be reduced in order to correctly simulate the observed *absolute* metal density [*Plane et al.*, 2018]. The Al MIF in WACCM is then set to vary with season and latitude in the same way as the Fe MIF [*Feng et al.*, 2013] i.e. an autumnal maximum and vernal minimum, increasing from essentially no variation at the equator to ±30% at the pole, with the same annual average input at all latitudes.

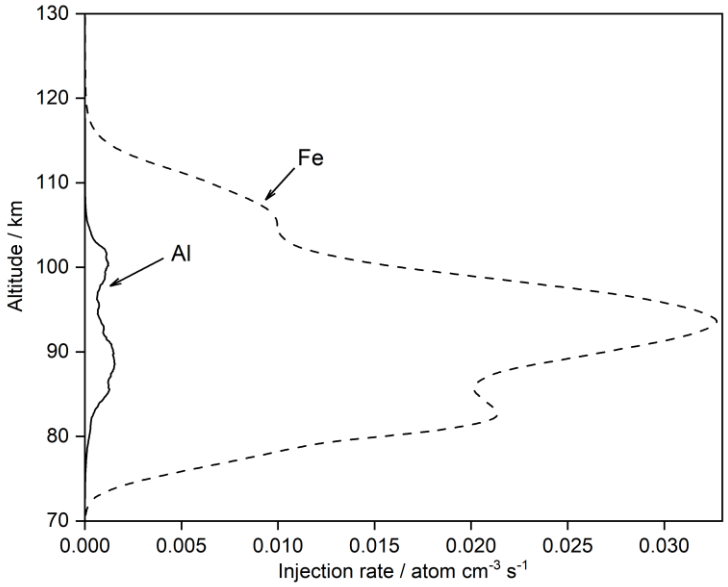

Figure 7. Global annual mean injection rates of Al and Fe from meteoric ablation. The injection profiles from [*Carrillo-Sánchez et al.*, 2020] have been divided by factor of 5.0.

4.3 Model results

Figure 8 shows the annual average vertical profiles of the major Al species at 54°N, the latitude of the lidar observations. As expected, Al^+ is the dominant species above 95 km. AlO and AlOH then occur in layers that peak around 89 and 86 km, respectively. $Al(OH)_2$ is also significant below 80 km once the atomic H concentration decreases significantly [*Plane et al.*, 2015], so that reaction R12 becomes very slow. Below 92 km, most of the Al is tied up as Al-containing polymers, which represent a surrogate for meteoric smoke particles (MSPs) (see Section 2.5).

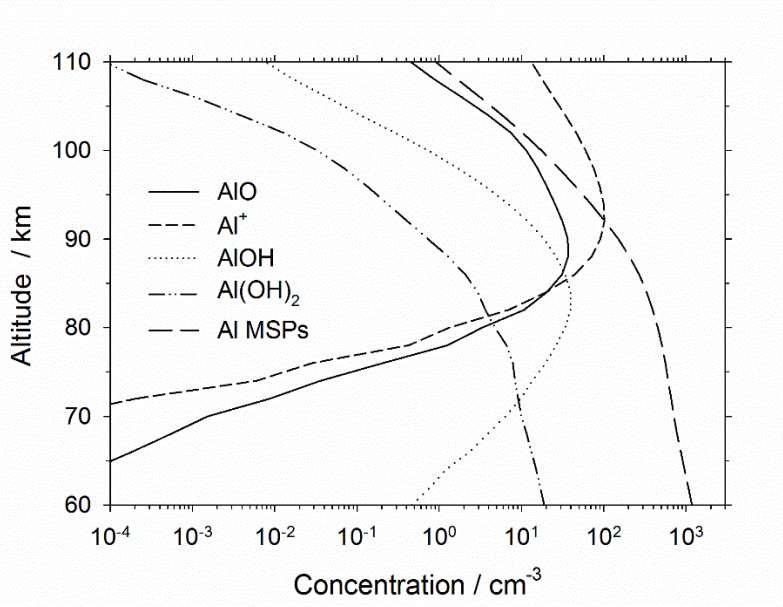

Figure 8. Annual average profiles of the major Al-containing species, simulated by WACCM-Al at 54^{o}N between 2004 and 2014. MSP = meteoric smoke particle.

Figure 9 (left panel) compares the vertical profile of Al^+ simulated by WACCM-Al with the geometric mean profiles from a set of eight mid- to high-latitude rocket-borne mass spectrometric measurements by Kopp and co-workers [*Meister et al.*, 1978; *Kopp et al.*, 1984; *Kopp et al.*, 1985a; *Kopp et al.*, 1985b; *Kopp*, 1997]. Details of these flights are provided in Table S5. The model results are the annual average simulated Al^+ profile at 0 LT for 54^{o}N. The observed Al^+ layer peaks around 92 - 94 km, with a geometric mean density of 40 cm^{-3} and geometric standard deviation from 20 – 100 cm^{-3}. The modeled layer peaks at 93 km, with a density close to 100 cm^{-3}. Given the paucity of observations, this level of agreement is satisfactory. Because the reaction of AlO^+ with O (R22) is relatively fast (Section 2.1.2) and O is a major species above 84 km, Al^+ is the major Al-containing ion by 2-5orders of magnitude between 85-110 km. Figure 9 (right panel) shows that the rocket-measured Fe^+:Al^+ ratio is also satisfactorily modeled between 86 and 104 km. The ratio is very close to the CABMOD-ZoDy estimate of the relative meteoric inputs, which is a factor of 2.8 larger than the CI ratio of the two metals.

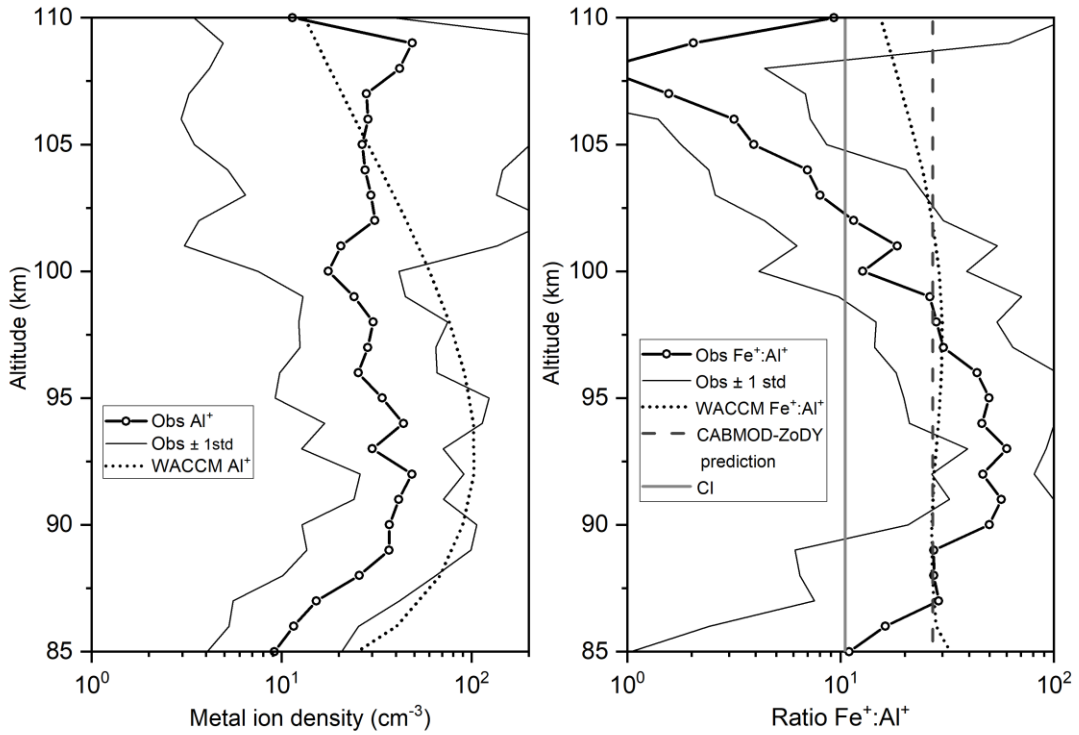

476

477 **Figure 9.** Left-hand panel: annual mean altitude profile of Al^+ at 0 LT, simulated by WACCM-
478 Al for Kühlungsborn (54ºN, 12ºE) (dotted line). The solid black line with open circles is the
479 geometric mean profile of Al^+, with the geometric standard deviation (1σ error limits, thin black
480 lines lines), for the eight rocket flights listed in Table S5. Right-hand panel: mean altitude profile
481 of the modeled Fe^+:Al^+ ratio (dotted line), compared with the measured ratio (solid black line
482 with open circles; geometric 1σ standard deviation shown by thin black lines lines). The Fe:Al
483 ablation ratio predicted by the CABMOD-ZoDY model and the CI ratio are shown by the
484 vertical lines on the plot.

485

486 Figure 10 shows the diurnal variation of Al^+, AlO and AlOH as a function of height during April
487 at 54ºN, in order to compare with the lidar measurements described in Section 3.1. The diurnal
488 variation of the vertical column densities of these species is shown in Figure S4. As expected,
489 Al^+ peaks between 13 and 17 UT because of the daytime increase in the concentrations of the
490 lower *E* region ions NO^+ and O_2^+, which charge transfer with AlO and AlOH (R18 – R20).

491 More interesting is the diurnal behavior of the neutral species AlO and AlOH, which are
492 essentially anti-correlated: AlO peaks during daytime, and AlOH at night. This behavior is
493 caused by the photolysis of AlOH (R17) to produced AlO either directly or via Al. The result is
494 that AlO varies between 10 and 20 cm^{-3} at night, but it increases to over 60 cm^{-3} between 13 and
495 20 UT. The nighttime level is consistent with the upper limit of 57 cm^{-3} determined from the
496 lidar observations (Section 3.1), and also with the concentration of ~5 cm^{-3} that is inferred from
497 the Al rocket release experiments (Section 3.2).

498

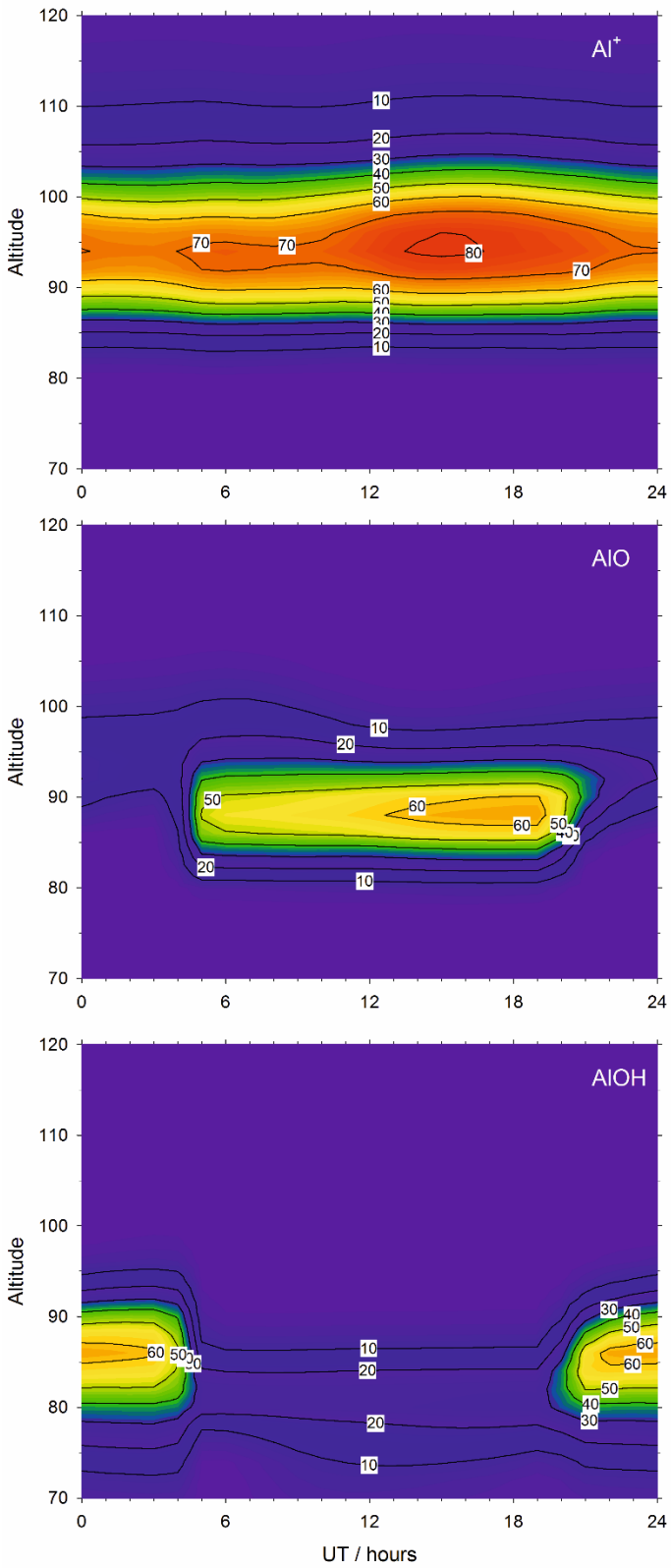

Figure 10. Hourly average vertical profiles of Al^+ (top panel), AlO (middle panel) and AlOH (bottom panel) for 54ºN during April (local time is ~1 hour ahead of Universal Time).

Figure 11 illustrates the variation with latitude and month of the vertical column densities of Al^+, AlO and AlOH. Al^+ shows little seasonal variation at low latitudes, but a 3-fold increase between winter and summer at mid- to high-latitudes, reflecting the change in ambient lower *E* region ionization. AlOH also demonstrates a strong (though opposite) annual cycle at high latitudes, increasing by a factor of ~6 from a mid-summer minimum in the continuously sunlit polar region to a mid-winter maximum in polar night. In contrast, AlO exhibits a semi-annual cycle at mid- to high-latitudes, peaking at the equinoxes. The reason is that after polar night, during which AlO is very low because most of the neutral Al is in the form of AlOH, photolysis causes a spring-time increase in AlO by a factor of ~3. However, moving into summer the AlO is reduced again by increased charge transfer with O_2^+ (R18), causing Al^+ to peak. The situation then reverses in the autumn. Note that the AlO is up to a factor of 2 times higher at the autumnal compared with the vernal equinox, because of the autumnal peak in the MIF [*Feng et al.*, 2013].

Figure S5 illustrates the seasonal/latitudinal variation of the centroid height and root-mean-square width of the AlO layer. Although the layer mostly peaks around 90 km, at high latitudes during polar night the peak increases to 98 km because AlOH is essentially a sink for neutral Al species below this in the absence of sunlight. In contrast, the mid-summer AlO layer at high latitudes still peaks around 90 km because now the removal of AlO is via charge transfer at higher altitudes. The RMS layer width is on average around 5 km, with a mid-summer minimum at polar latitudes of 3.6 km because of the ionization of the top-side of the AlO layer.

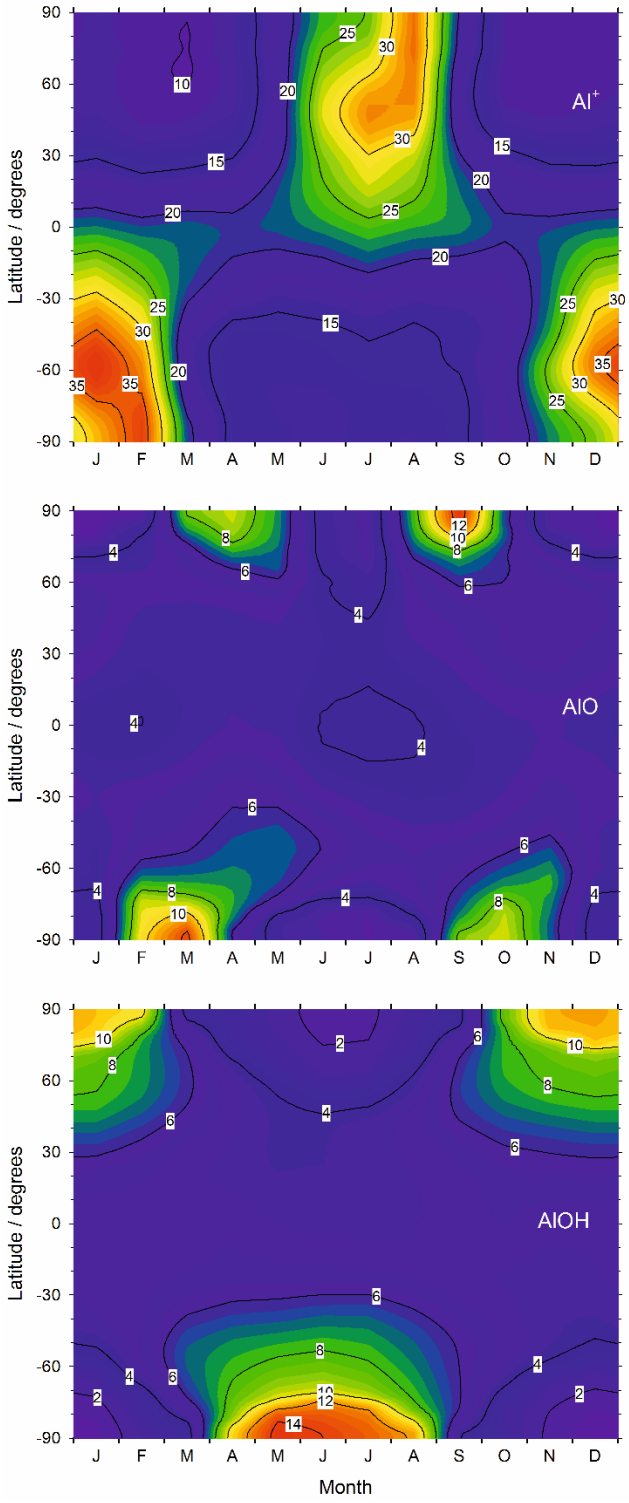

Figure 11. Seasonal/latitudinal variations of the column abundances of AlO, AlOH and Al^+ (units: 10^7 cm^{-2}), averaged from 2004 to 2014.

5 Conclusions

In this study we describe a comprehensive Al chemistry network, constructed from a set of neutral and ion-molecule reactions measured previously in our laboratory [*Daly et al.*, 2019; *Mangan et al.*, 2020], as well as the reactions of AlO^+ with O and CO (R22 and R23) reported as part of the present study. Additional reaction rate coefficients are estimated by using electronic structure theory to explore the relevant potential energy surfaces. The Al reaction network was then incorporated into the WACCM chemistry-climate model, along with a new MIF for Al [*Carrillo-Sánchez et al.*, 2020].

We also report the first attempt, to our knowledge, to directly observe the AlO layer in the MLT. Although the lidar observations did not detect a layer, an upper limit of only 57 cm^{-3} for the AlO density was determined. This sets an important benchmark for future observations. A rough estimate for AlO of around 5 cm^{-3} was obtained from the rate of decay of AlO chemiluminescence from rocket-borne grenade releases. Both of these types of atmospheric measurements apply to nighttime. However, the WACCM-Al model indicates that AlO should be a factor of ~6 times higher during daytime, because of photolysis of AlOH, which is the other major neutral Al-containing molecule. Of course, this result depends on the accuracy of the calculated photolysis rate of AlOH (Section 2.3), and it is essential that this is measured in the future. Lidar measurements during twilight, when photolysis of AlOH in the MLT is still occurring but the solar terminator is above the troposphere so that the amount of scattered sunlight is reduced, would offer the best chance of detecting AlO. This is particularly the case at high latitudes during spring or autumn (e.g. at 69°N, 3 hrs of twilight measurements could be made on J112 or J253), when the AlO density should also be highest (Figure 11).

Acknowledgments

This work was supported by Natural Environment Research Council grant NE/P001815/1. S.M.D. was supported by a studentship from the NERC SPHERES Doctoral Training Program. The rocket flight data was kindly provided by E. Kopp (University of Bern). The WACCM-Al and WACCM-Fe models were performed on the University of Leeds Advanced Research Computer (ARC4).There are no conflicts of interest for any author.

Data Availability Statement

The version cesm2_1_3 model and input data are provided by the National Centre for Atmospheric Research (http://www.cesm.ucar.edu/models/cesm2/release_download.html). The WACCM-Al and WACCM-Fe models and output are archived in the Petabyte Environmental Tape Archive and Library at the University of Leeds via https://petal.leeds.ac.uk/. The data is available at http://doi.org/10.5281/zenodo.4066748.

References

Alpers, M., J. Höfffner, and U. von Zahn (1996), Upper atmosphere Ca and Ca^+ at mid-latitudes: First simultaneous and common-volume lidar observations, *Geophys. Res. Lett.*, *23*, 567-570.

Asplund, M., N. Grevesse, A. J. Sauval, and P. Scott (2009), The Chemical Composition of the Sun, in *Ann. Rev. Astron. Astrophys.*, edited by R. Blandford, J. Kormendy and E. van Dishoeck, pp. 481-522, Annual Reviews, Palo Alto, doi:10.1146/annurev.astro.46.060407.145222.

Bai, X., and T. C. Steimle (2020), The Stark Effect, Zeeman Effect, and Transition Dipole Moments for the $B^2\Sigma^+ - X^2\Sigma^+$ Band of Aluminum Monoxide, AlO, *Astrophys. J.*, *889*, art. no.: 147.

Bauernschmitt, R., and R. Ahlrichs (1996), Treatment of electronic excitations within the adiabatic approximation of time dependent density functional theory, *Chem. Phys. Lett.*, *256*, 454-464.

Bones, D. L., S. Daly, T. P. Mangan, and J. M. C. Plane (2020), A Study of the reactions of Ni^+ and NiO^+ ions relevant to planetary upper atmospheres, *Phys. Chem. Chem. Phys.*, *22* 8940-8951.

Bones, D. L., J. M. C. Plane, and W. Feng (2016), Dissociative Recombination of FeO^+ with Electrons: Implications for Plasma Layers in the Ionosphere, *J. Phys. Chem. A*, *120*, 1369-1376.

Borovička, J., and A. A. Berezhnoy (2016), Radiation of molecules in Benešov bolide spectra, *Icarus*, *278*, 248–265.

Carrillo-Sánchez, J. D., J. C. Gómez-Martín, D. L. Bones, D. Nesvorný, P. Pokorný, M. Benna, G. J. Flynn, and J. M. C. Plane (2020), Cosmic dust fluxes in the atmospheres of Earth, Mars, and Venus, *Icarus*, *335*, art. no.: 113395.

Carrillo-Sánchez, J. D., D. Nesvorný, P. Pokorný, D. Janches, and J. M. C. Plane (2016), Sources of cosmic dust in the Earth's atmosphere, *Geophys. Res. Lett.*, *43*, 11,979-911,986.

Clemmer, D. E., M. E. Weber, and P. B. Armentrout (1992), Reactions of $Al^+(^1S)$ with NO_2, N_2O and CO_2 - thermochemistry of AlO and AlO^+, *J. Phys. Chem.*, *96*, 10888-10893.

Daly, S. M., D. L. Bones, and J. M. C. Plane (2019), A study of the reactions of Al^+ ions with O_3, N_2, O_2, CO_2 and H_2O: influence on Al^+ chemistry in planetary ionospheres, *Phys. Chem. Chem. Phys.*, *21*, 14080-14089.

Daly, S. M., W. Feng, T. P. Mangan, M. Gerding, and J. M. C. Plane (2020), The Meteoric Ni Layer in the Upper Atmosphere, *J. Geophys. Res. - Space Phys.*, *125*, art. no.: e2020JA028083.

Danabasoglu, G., J.-F. Lamarque, J. Bacmeister, D. A. Bailey, A. K. DuVivier, J. Edwards, L. K. Emmons, J. Fasullo, R. R. Garcia, A. Gettelman, et al. (2020), The Community Earth System Model version 2 (CESM2), *J. Adv. Mod. Earth Sys.*, *12*, art. no.: e2019MS001916.

Evans, W. F. J., R. L. Gattinger, A. L. Broadfoot, and E. J. Llewellyn (2011), The observation of chemiluminescent NiO* emissions in the laboratory and in the night airglow, *Atmos. Chem. Phys.*, *11*, 9595-9603.

Feng, W., D. R. Marsh, M. P. Chipperfield, D. Janches, J. Höffner, F. Yi, and J. M. C. Plane (2013), A global atmospheric model of meteoric iron, *J. Geophys. Res.-Atmos.*, *118*, 9456-9474.

Florescu-Mitchell, A. I., and J. B. A. Mitchell (2006), Dissociative recombination, *Phys. Reports*, *430*, 277-374.

Frisch, M. J., G. W. Trucks, H. B. Schlegel, G. E. Scuseria, M. A. Robb, J. R. Cheeseman, G. Scalmani, V. Barone, G. A. Petersson, H. Nakatsuji, et al. (2016), Gaussian 16, Revision B.01, edited, Gaussian, Inc., Wallingford, CT, USA.

Gardner, C. S., A. Z. Liu, and Y. Guo (2017), Vertical and horizontal transport of mesospheric Na: Implications for the mass influx of cosmic dust, *J. Atmos. Sol. Terr. Phys.*, *162*, 192-202.

Gerding, M., M. Alpers, U. von Zahn, R. J. Rollason, and J. M. C. Plane (2000), Atmospheric Ca and Ca^+ layers: Midlatitude observations and modeling, *J. Geophys. Res.-Atmos.*, *105*, 27131-27146.

Gerding, M., S. Daly, and J. M. C. Plane (2019), Lidar Soundings of the Mesospheric Nickel Layer Using Ni(^{3}F) and Ni(^{3}D) Transitions, *Geophys. Res. Lett.*, *46*, 408-415.

Gerding, M., M. Kopp, J. Höffner, K. Baumgarten, and F.-J. Lübken (2016), Mesospheric temperature soundings with the new, daylight-capable IAP RMR lidar, *Atmos. Meas. Tech. , 9*, 3707-3715.

Gerrard, A. J., T. J. Kane, J. P. Thayer, C. S. Ruf, and R. L. Collins (2001), Consideration of non-Poisson distributions for lidar applications, *Appl. Opt.*, *40*, 1488-1492.

Gettelman, A., M. J. Mills, D. E. Kinnison, R. R. Garcia, A. K. Smith, D. R. Marsh, S. Tilmes, F. Vitt, C. G. Bardeen, J. McInerny, et al. (2019), The Whole Atmosphere Community Climate Model Version 6 (WACCM6), *124*, 12380-12403.

Gole, J. L., and C. E. Kolb (1981), On the upper atmospheric chemiluminescent emission observed upon release of aluminum vapor and its compounds, *J. Geophys. Res.*, *86*, 9125-9136.

Golomb, D., and J. H. Brown (1976), Chemiluminescence of trimethyl aluminum in active oxygen and nitrogen, *Combust. Flame*, *27*, 383-389.

Golomb, D., O. Harang, and F. P. DelGreco (1967), Upper atmosphere densities and temperatures at 105–165 kilometers from diffusion and spectral intensity of AlO trails, *J. Geophys. Res.*, *72*, 2365-2370.

Gómez-Martín, J. C., and J. M. C. Plane (2017), Reaction Kinetics of CaOH with H and O2 and O2CaOH with O: Implications for the Atmospheric Chemistry of Meteoric Calcium, *ACS Earth Space Chem.*, *1*, 431-441.

Gómez-Martín, J. C., C. Seaton, M. P. Miranda, and J. M. C. Plane (2017), The Reaction between Sodium Hydroxide and Atomic Hydrogen in Atmospheric and Flame Chemistry, *J. Phys. Chem. A*, *121*, 7667−7674.

Gómez Martín, J. C., S. M. Daly, J. S. A. Brooke, and J. M. C. Plane (2017), Absorption cross sections and kinetics of formation of AlO at 298K, *Chem. Phys. Lett.*, *675*, 56-62.

Grebowsky, J. M., and A. C. Aikin (2002), In Situ Measurements of Meteoric Ions, in *Meteors in the earth's atmosphere*, edited by E. Murad and I. P. Williams, pp. 189-214, Cambridge University Press, Cambridge.

Jessberger, E. K., T. Stephan, D. Rost, P. Arndt, M. Maetz, F. J. Stadermann, D. E. Brownlee, J. P. Bradley, and G. Kurat (2001), Properties of Interplanetary Dust: Information from Collected Samples, in *Interplanetary Dust*, edited by E. Grün, B. Å. S. Gustafson, S. Dermott and H. Fechtig, pp. 253-294, Springer Berlin Heidelberg, Berlin, Heidelberg, doi:10.1007/978-3-642-56428-4_6.

Johnson, E. R. (1965), Twilight resonance radiation of AlO in the upper atmosphere, *J. Geophys. Res.*, *70*, 1275-1277.

Kopp, E. (1997), On the abundance of metal ions in the lower ionosphere, *J. Geophys. Res.-Space Phys.*, *102*, 9667-9674.

Kopp, E., L. André, and L. G. Smith (1985a), Positive ion composition and derived particle heating in the lower auroral ionosphere, *J. Atmos. Sol. Terr. Phys.*, *47*, 301-308.

Kopp, E., P. Eberhardt, U. Herrmann, and L. G. Björn (1985b), Positive ion composition of the high-latitude summer D region with noctilucent clouds, *J. Geophys. Res.-Atmos.*, *90*, 13041-13053.

Kopp, E., H. Ramseyer, and L. G. Björn (1984), Positive ion composition and electron density in a combined auroral and NLC event, *Adv. Space Res.*, *4*, 157-161.

Krankowsky, D., F. Arnold, H. Wieder, and J. Kissel (1972), The elemental and isotopic abundance of metallic ions in the lower E-region as measured by a cryogenically pumped quadrupole mass spectrometer, *Int. J. Mass Spectr. Ion Phys.*, *8*, 379-390.

Langowski, M. P., C. von Savigny, J. P. Burrows, W. Feng, J. M. C. Plane, D. R. Marsh, D. Janches, M. Sinnhuber, A. C. Aikin, and P. Liebing (2015), Global investigation of the Mg atom and ion layers using SCIAMACHY/Envisat observations between 70 and 150 km altitude and WACCM-Mg model results, *Atmos. Chem. Phys.*, *15*, 273-295.

Mangan, T. P., J. M. Harman-Thomas, R. E. Lade, K. M. Douglas, and J. M. C. Plane (2020), Kinetic study of the reactions of AlO and OAlO relevant to planetary mesospheres, *ACS Earth Space Chem.*, *under review*.

Marsh, D. R., D. Janches, W. Feng, and J. M. C. Plane (2013), A global model of meteoric sodium, *J. Geophys. Res.-Atmos.*, *118*, 11,442-411,452.

Meister, J., P. Eberhardt, U. Herrmann, E. Kopp, M. A. Hidalgo, and J. Sechrist, CF. (1978), D-region ion composition during the winter anomaly campaign on January 8, 1977, *Space Res. XVIII*, 155-159.

Molina, L. T., and M. J. Molina (1986), Absolute absorption cross sections of ozone in the 185- to 350-nm wavelength range, *J. Geophys. Res.-Atmos.*, *91*, 14501-14508.

Montgomery, J. A., M. J. Frisch, J. W. Ochterski, and G. A. Petersson (2000), A complete basis set model chemistry. VII. Use of the minimum population localization method, *J. Chem. Phys.*, *112*, 6532-6542.

Nesvorný, D., D. Janches, D. Vokrouhlický, P. Pokorný, W. F. Bottke, and P. Jenniskens (2011), Dynamical Model for the Zodiacal Cloud and Sporadic Meteors, *Astrophys. J.*, *743*, 129.

Picone, J. M., A. E. Hedin, D. P. Drob, and A. C. Aikin (2002), NRLMSISE-00 empirical model of the atmosphere: Statistical comparison and scientific issues, *J. Geophys. Res.-Atmos.*, *107*, art. no.: 1468.

Plane, J. M. C. (2003), Atmospheric chemistry of meteoric metals, *Chem. Rev.*, *103*, 4963-4984.

Plane, J. M. C., W. Feng, E. Dawkins, M. P. Chipperfield, J. Höffner, D. Janches, and D. R. Marsh (2014), Resolving the strange behavior of extraterrestrial potassium in the upper atmosphere, *Geophys. Res. Lett.*, *41*, 4753-4760.

Plane, J. M. C., W. Feng, and E. C. M. Dawkins (2015), The Mesosphere and Metals: Chemistry and Changes, *Chem. Rev.*, *115*, 4497-4541.

Plane, J. M. C., W. Feng, J. C. Gómez Martín, M. Gerding, and S. Raizada (2018), A new model of meteoric calcium in the mesosphere and lower thermosphere, *Atmos. Chem. Phys.*, *18*, 14799-14811.

Plane, J. M. C., J. C. Gomez-Martin, W. H. Feng, and D. Janches (2016), Silicon chemistry in the mesosphere and lower thermosphere, *J. Geophys. Res.-Atmos.*, *121*, 3718-3728.

Roberts, B. C., and M. F. Larsen (2014), Structure function analysis of chemical tracer trails in the mesosphere-lower thermosphere region, *J. Geophys. Res.-Atmos.*, *119*, 6368-6375.

Rosenberg, N. W., D. Golomb, and E. F. Allen Jr. (1964), Resonance Radiation of Al0 from Trimethyl Aluminum Released into the Upper Atmosphere, *J. Geophys. Res.*, *69*, 1451-1454.

Saran, D. V., T. G. Slanger, W. Feng, and J. M. C. Plane (2011), FeO emission in the mesosphere: Detectability, diurnal behavior, and modeling, *J. Geophys. Res.-Atmos.*, *116*, art. no.: D12303.

Self, D. E., and J. M. C. Plane (2003), A kinetic study of the reactions of iron oxides and hydroxides relevant to the chemistry of iron in the upper mesosphere, *Phys. Chem. Chem. Phys.*, *5*, 1407-1418.

Sikorska, C., and P. Skurski (2009), Cationic and anionic daughters of AlOH and GaOH. An *ab initio* study, *Chem. Phys. Lett.*, *477*, 259–265.

Smith, I. W. M. (1980), *Kinetics and Dynamics of Elementary Gas Reactions*, Butterworths, London.

Tilgner, C., and U. von Zahn (1988), Average properties of the sodium density distribution as observed at 69°N latitude in winter, *J. Geophys. Res.-Atmos.*, *93*, 8439-8454.

Tobiska, W. K., T. Woods, F. Eparvier, R. Viereck, L. Floyd, D. Bouwer, G. Rottman, and O. R. White (2000), The SOLAR2000 empirical solar irradiance model and forecast tool, *J. Atmos. Sol. Terr. Phys.*, *62*, 1233–1250.

Trabelsi, T., and J. S. Francisco (2018), Is AlOH the Astrochemical Reservoir Molecule of AlO?: Insights from Excited Electronic States, *Astrophys. J.*, *863*, art. no.: 139.

Troe, J. (1985), Statistical adiabatic channel model of ion-neutral dipole capture rate constants, *Chem. Phys. Lett.*, *122*, 425-430.

Viehl, T. P., J. M. C. Plane, W. Feng, and J. Höffner (2016), The photolysis of FeOH and its effect on the bottomside of the mesospheric Fe layer, *Geophys. Res. Lett.*, *43*, 1373-1381.

Figure Captions

Figure 1. Schematic diagram of meteor-ablated Al chemistry in the MLT. Ionized and neutral Al species are contained in blue and green boxes, respectively. Blue arrows indicate reactions measured previously, and the red arrow shows the reactions measured in the present study.

Figure 2. Fractional recovery of $[Al^+]$ plotted against the ratio of $[CO]/[O_3]$ in the flow tube. The solid points are the experimental data and the model fit is the solid black line, with the dashed lines illustrating the $\pm 1\sigma$ uncertainty in k_{23}. Conditions: 1 Torr, T = 294 K.

Figure 3. $[Al^+]$ as a function of $[O_3]$ in the presence of O (open circles, $[O] = 1.36 \times 10^{13}$ molecule cm^{-3}) and with the O discharge switched off (solid circles). The solid lines are model fits through the experimental data, and the dashed lines denote the $\pm 1\sigma$ uncertainty in k_{22}. Conditions: 1 Torr, T = 294 K.

Figure 4. Reaction potential energy surfaces calculated at the CBS-QB3 level of theory: (a) $OAlO_2$ + H; (b) $OAlO_2 + H_2O$; (c) $Al(OH)_2$ + H

Figure 5. Absorption cross section of AlOH calculated at the TD-B3LYP//6-311+g(2d,p) level of theory. The dashed line indicates the threshold for photodissociation to Al + OH or AlO + H.

Figure 6. Integrated backscatter profile of lidar soundings during April 2017 on a log scale. (a) 484 nm lidar (blue line) and RMR lidar (green), after background subtraction. The dashed line is the 484 nm background signal measured between 120 and 150 km. The purple line is the extrapolated Rayleigh backscatter above 80 km. (b) The 484 nm lidar – background (blue line) and the extrapolated Rayleigh signal (purple line) on a linear scale. (c) Residual signal after the background and extrapolated Rayleigh backscatter are subtracted from the 484 nm signal. The red line is the 3σ photon noise level. The altitude resolution is 200 m.

Figure 7. Global annual mean injection rates of Al and Fe from meteoric ablation. The injection profiles from [*Carrillo-Sánchez et al.*, 2020] have been divided by factor of 5.0.

Figure 8. Annual average profiles of the major Al-containing species, simulated by WACCM-Al at 54ºN between 2004 and 2014. MSP = meteoric smoke particle.

Figure 9. Left-hand panel: annual mean altitude profile of Al^+ at 0 LT, simulated by WACCM-Al for Kühlungsborn (54ºN, 12ºE) (dotted line). The solid black line with open circles is the geometric mean profile of Al^+, with the geometric standard deviation (1σ error limits, thin black lines lines), for the eight rocket flights listed in Table S5. Right-hand panel: mean altitude profile of the modeled Fe^+:Al^+ ratio (dotted line), compared with the measured ratio (solid black line with open circles; geometric 1σ standard deviation shown by thin black lines lines). The Fe:Al ablation ratio predicted by the CABMOD-ZoDY model and the CI ratio are shown by the vertical lines on the plot.

Figure 10. Hourly average vertical profiles of Al^+ (top panel), AlO (middle panel) and AlOH (bottom panel) for 54ºN during April (local time is ~1 hour ahead of Universal Time).

Figure 11. Seasonal/latitudinal variations of the column abundances of AlO, AlOH and Al^+ (units: 10^7 cm^{-2}), averaged from 2004 to 2014.

Tables

Table 1. Aluminum chemistry in the MLT